scientific reports

Check for updates

OPEN

Analysis of the long-term sealing integrity of cement sheath in CO_2 storage wells

Kaide Zhao[1,2,3], Shuangjin Zheng[1,2,3]✉, Hu Meng[1,2,3], Zhijie Ren[4], Yun Zou[5] & Dengwei Fu[6]

CO_2 geological storage is widely regarded as one of the most technically mature and large-scale options for emissions reduction within CCUS (Carbon Capture, Utilization and Storage) technologies. However, CO_2 corrosion and long-term injection/storage operations pose significant threats to the sealing integrity of cement sheaths in wellbores. Existing studies predominantly rely on numerical simulations to analyze the mechanical response on cement sheath under temperature–pressure conditions, neglecting the corrosion of cement sheath. However, there is a notable lack of theoretical computation models specifically for cement sheaths containing the coupled effects of corrosion and stress. This study establishes a mechanical model of the casing-CCS (corroded cement sheath)-formation assembly based on elastoplastic theory, incorporating thick-walled cylinder theory and the Mohr–Coulomb criterion. The model is solved using MATLAB to quantify the stress-displacement response of CCS during injection and storage. Results indicate that CO_2 corrosion significantly increases the complexity of the stress state in the cement sheath and the risk of sealing failure. For a representative injection pressure of 60 MPa, introducing a 5 mm corroded layer increases the predicted micro-annulus aperture at the primary casing-cement interface from 0.0238 mm to 0.0519 mm after unloading (an increase of 118%). When the injection pressure varies from 40 to 100 MPa, the micro-annulus aperture grows from 0.0211 mm to 0.1113 mm, whereas increasing the CSCL thickness from 5 to 30 mm only enlarges it from 0.0519 mm to 0.0579 mm (11.5%). In contrast, increasing casing wall thickness from 7.5 mm to 17.5 mm reduces the maximum radial stress in the cement sheath from -28.88 MPa to -18.68 MPa and decreases the micro-annulus aperture from 0.1829 mm to 0.0413 mm. This study provides a theoretical foundation for optimizing wellbore design in CCUS projects.

Keywords Corroded cement sheath, CCUS, CO_2 corrosion, Sealing integrity, Micro-annulus

Abbreviations

CCUS	Carbon capture, utilization and storage
CCS	Corroded cement sheath
CSCL	Cement sheath corroded layer
CSIL	Cement sheath intact layer

CO_2 geological storage, a pivotal component of CCUS (Carbon Capture, Utilization, and Storage), is widely considered one of the most mature and economically viable pathways for achieving large-scale CO_2 emission reductions.[1–3] CO_2 geological storage typically involves injecting CO_2 into subsurface geological formations, such as deep saline aquifers, depleted hydrocarbon reservoirs, or unmineable coal seams.[4–8] These formations exhibit effective sealing properties. Specifically, utilizing depleted hydrocarbon reservoirs for CO_2 storage is currently a widely adopted approach. However, it poses significant challenges to the sealing integrity of cement sheaths in existing wellbores.[9–12] Ensuring cement sheath integrity in storage wells is critical to achieving long-term effective CO_2 storage, and accurate elucidation of the seal failure mechanisms under long-term CO_2 injection and storage is imperative.

[1]Hubei Key Laboratory of Oil and Gas Drilling and Production Engineering, Yangtze University), Wuhan 430100, China. [2]School of Petroleum Engineering, Yangtze University, Wuhan 430100, China. [3]State Key Laboratory of Low Carbon Catalysis and Carbon Dioxide Utilization (Yangtze University), Wuhan 430100, China. [4]Oil Production Technology Research Institute, PetroChina LIAOHE Oilfield Company, Panjin 124010, China. [5]Golden Sea Oil Production Plant, PetroChina LIAOHE Oilfield Company, Panjin 124010, China. [6]PetroChina Xinjiang Oilfield Company, Karamay 834000, China. ✉email: 2023710278@yangtzeu.edu.cn

Under CO_2 injection and storage conditions in storage wells, cyclic loading and unloading of wellbore pressure may induce zonal isolation failure of the cement sheath.[13–15] Primary failure modes include debonding at the first and second bonding interfaces and structural damage to the cement matrix. Addressing the prominent issue of zonal isolation integrity failure in cement sheaths, domestic and international scholars have conducted extensive investigations into failure mechanisms of both the cement matrix and bonding interfaces through integrated approaches including theoretical analysis, laboratory physical simulations, and numerical modeling. Current research on stress and displacement calculations for conventional casing-cement sheath-formation assemblies based on elastoplastic mechanics theory is well-established, particularly regarding the cement sheath where extensive prior research exists. Deng et al. derived analytical solutions for stress distribution in the casing-cement sheath-formation assembly under both linearly elastic and fully plastic states based on multi-layered thick-walled cylinder theory, and further analyzed the compatibility between cement mechanical parameters and sheath integrity under cyclic internal pressure loading.[16] Chu et al. established a cement sheath assembly model based on the Mohr–Coulomb criterion. Their study revealed that micro-annulus formation is jointly determined by both loading and unloading processes, concluding that the primary cementing interface is more susceptible to micro-annulus generation. Furthermore, they quantitatively calculated the magnitude of the micro-annulus.[17–19] Scholars have further investigated cement sheath failure under cyclic internal pressure conditions, concluding that the accumulation of residual strain within the cement sheath is the critical factor triggering micro-annulus generation.[20,21] Additionally, scholars have developed specialized evaluation apparatus to assess cement sheath sealing integrity under varying wellbore conditions and formation disturbances. For example, shale gas simulation devices with alternating load capabilities are employed to evaluate interface sealing performance across different geological formations. Through integrated theoretical modeling, these studies propose specific mechanical property requirements (elastic modulus and Poisson's ratio) for cement sheaths under diverse operational scenarios.[22–24].

In CO_2 long-term storage wells, the cement sheath is subjected not only to cyclic casing internal pressure loads but also to prolonged CO_2 erosion. During the initial stage of CO_2 intrusion, the formation of calcium carbonate reduces the porosity and permeability of the cement while increasing its mechanical strength. However, as the corrosion period extends, the dissolution of calcium carbonate leads to increased porosity and permeability, accompanied by a significant degradation in mechanical strength.[25,26] Wu et al. conducted mechanical performance experiments on CCS (corroded cement sheath), demonstrating that short-term corrosion enhances cement strength, whereas prolonged exposure gradually deteriorates its mechanical properties.[27] Gu et al. experimentally investigated the corrosion damage evolution of cement under CO_2 geological storage conditions, analyzing the progression of microstructural changes and macroscopic mechanical properties over corrosion time. Their study established a correlation between cement corrosion depth and exposure duration.[28–30].

In CO_2 long-term storage wells, the cement sheath is subjected not only to cyclic casing internal pressure and temperature but also to prolonged CO_2 attack. A number of recent studies have employed numerical simulations to investigate the mechanical response of cement and cement-formation systems under CO_2 exposure or carbonation, often incorporating damage evolution, permeability changes, and interface failure. However, these works predominantly rely on finite-element or finite-difference discretization and seldom provide closed-form elastoplastic solutions for the casing-cement-formation assembly that explicitly include a corroded cement layer. There is still a notable lack of analytical computation models that couple corrosion-induced changes in cement properties with internal pressure loading/unloading and directly quantify micro-annulus formation at the casing-cement interface.[31,32] The present work fills this gap by developing a casing-CCS-formation mechanical model based on thick-walled cylinder theory and the Mohr–Coulomb criterion, in which a CO_2-corroded cement layer is explicitly represented; deriving closed-form solutions for stress and displacement during injection and subsequent pressure unloading, including the micro-annulus aperture at the primary casing-cement interface; and applying the model to systematically evaluate how injection pressure, corrosion layer thickness, and casing wall thickness influence plastic yielding and the sealing integrity of the cement sheath in CO_2 storage wells. It further analyzes the integrity failure and plastic deformation behavior of CCS under the coupled influence of CO_2 corrosion and internal pressure.

Development of an Elastoplastic Model for Casing-CCS-Formation Assembly

Upon completion of cementing operations, the annular space between the casing and formation is filled with a cement sheath, creating a tightly bonded assembly. With negligible axial slippage at both the casing-cement and cement-formation interfaces, this configuration can be analyzed using thick-walled cylinder theory.[33] Assuming the casing and formation behave as perfectly elastic bodies, while the corrosion-affected cement sheath exhibits ideal elastoplastic behavior, a mechanical model of the casing-CCS-formation assembly under uniform in-situ stress is established.[17] The schematic diagram of the model structure is shown in Fig. 1.

Under long-term CO_2 injection and geological storage conditions, CO_2 progressively corrodes the cement sheath, resulting in distinct corroded and intact zones. The mechanical properties of cement sheaths with corroded layers significantly differ from those of uncorroded layers. To analyze the mechanical behavior of CO_2 storage well cement sheaths containing corroded layers under downhole complex loading, a reconstructed mechanical model is essential. The Mohr–Coulomb criterion is adopted to determine whether the cement sheath enters a plastic state, expressed as:[16]

$$\frac{1}{2}(\sigma_1 - \sigma_3) + \frac{1}{2}(\sigma_1 + \sigma_3)\sin\phi = C \tag{1}$$

where is the material cohesion , MPa; φ is the material internal friction angle ,°; is the maximum principal stress, MPa; is the minimum principal stress, MPa.

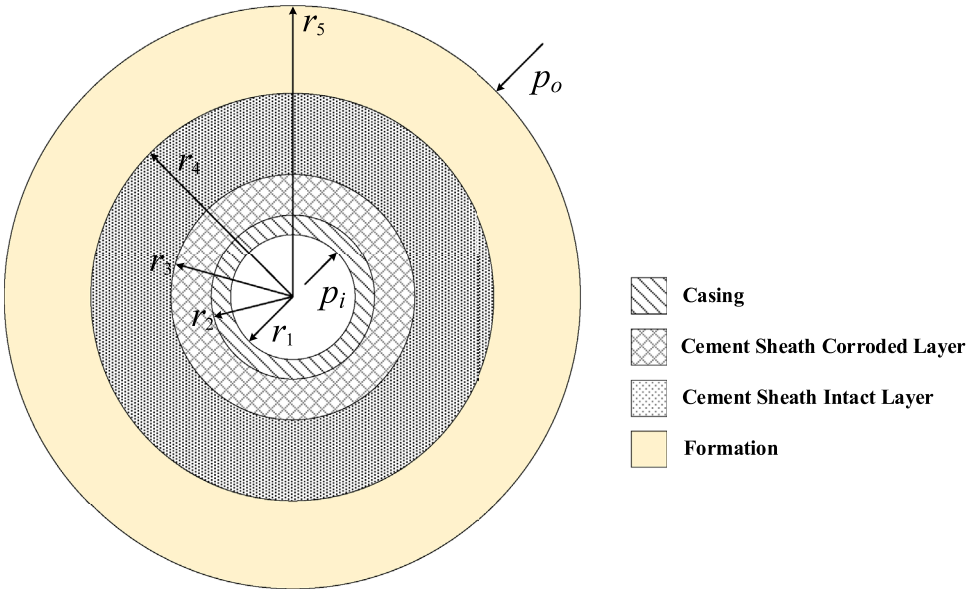

Fig. 1. Diagram of the mechanical model structure.

Stress and displacement of casing during CO_2 injection

Derivation of stress distribution at any point in casing based on Lame's Formula:

$$\begin{cases} \sigma_{rc} = \frac{r_2^2 r_1^2 (P_1 - P_i)}{r_2^2 - r_1^2} \frac{1}{r^2} + \frac{r_1^2 P_i - r_2^2 P_1}{r_2^2 - r_1^2} \\ \sigma_{\theta c} = \frac{r_1^2 P_i - r_2^2 P_1}{r_2^2 - r_1^2} - \frac{r_2^2 r_1^2 (P_1 - P_i)}{r_2^2 - r_1^2} \frac{1}{r^2} \end{cases} \tag{2}$$

Derivation of radial displacement at any point in casing based on relevant displacement equations:

$$\begin{aligned} u_{co} &= \frac{1+v_1}{E_1} \frac{2(1-v_1) r_1^2 r_2}{r_2^2 - r_1^2} P_i - \frac{1+v_1}{E_1} \frac{r_1^2 r_2 + (1-2v_1) r_2^3}{r_2^2 - r_1^2} P_1 \\ &= S_1 P_i - S_2 P_1 \end{aligned} \tag{3}$$

where σ_{rc} is the radial stress of casing, MPa; $\sigma_{\theta c}$ is the circumferential stress of casing, MPa; P_i is the internal pressure during CO_2 injection, MPa; P_1 is the interfacial contact stress at the casing outer boundary, MPa; r_1 is the inner diameter of casing, mm; r_2 is the outer diameter of casing, mm; u_{co} is the radial displacement of casing, mm; E_1 is the elastic modulus of casing, GPa; v_1 is the Poisson's ratio of casing, dimensionless; S_1 and S_2 are coefficients in the radial displacement equation, dimensionless.

Stress and displacement of the CSCL (Cement Sheath Corroded Layer) during CO_2 injection

Under prolonged CO_2 corrosion, the mechanical strength of the cement sheath significantly degrades, resulting in substantially weaker strength in the corroded zone compared to the uncorroded zone. Therefore, during CO_2 injection, when subjected to casing internal pressure, the cement sheath corroded zone enters the elastoplastic stage prior to the uncorroded zone. Only when the corroded zone reaches the fully plastic stage will the uncorroded zone transition into the elastoplastic stage under higher casing internal pressure. Here, taking two working conditions as examples—Condition 1: the CSCL enters the elastoplastic stage while the CSIL(cement sheath intact layer) remains fully elastic, and Condition 2: the CSCL enters the fully plastic stage while the CSIL remains fully elastic—the stress and displacement responses of each assembly in the mechanical model during the CO_2 injection phase are introduced. The structural behaviors under these two working conditions are illustrated in Fig. 2: (a) represents the structural mechanical characteristics of the CSCL in the elastoplastic stage, and (b) represents the structural mechanical characteristics of the CSIL in the elastoplastic stage.

For the fully elastic stage of the CSCL, the stress and displacement derivation formulas are identical to those of the casing.

Elastoplastic stage of the CSCL

(1) Plastic zone in the CSCL.

Stress distribution in the plastic zone of CSCL can be obtained by Eq. (4), When $r = r_{sc}$, $\sigma_{rscp} = -P_{sc}$.

$$\begin{cases} \sigma_{rscp} = C \cot\varphi [1 - \left(1 + \frac{P_1}{C \cot\varphi}\right) \left(\frac{r}{r_2}\right)^{N-1}] \\ \sigma_{\theta scp} = C \cot\varphi [1 - N \left(1 + \frac{P_1}{C \cot\varphi}\right) \left(\frac{r}{r_2}\right)^{N-1}] \end{cases} \tag{4}$$

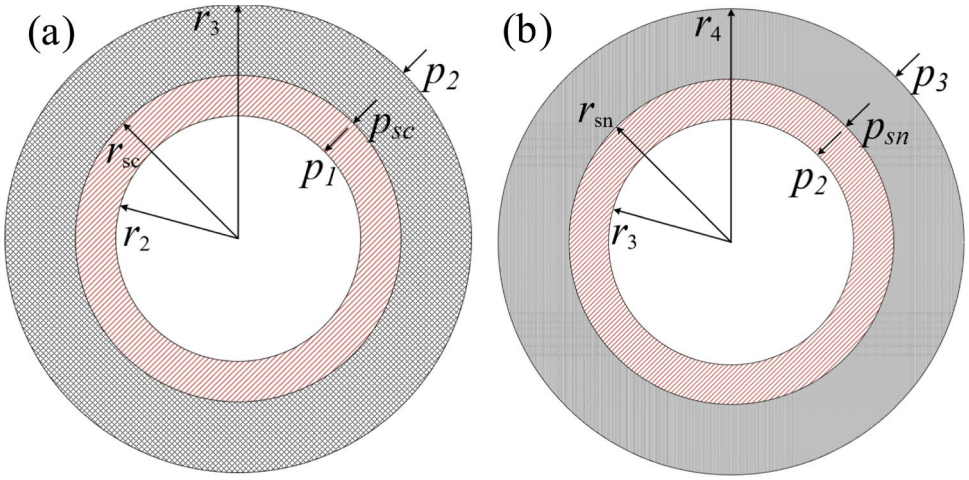

Fig. 2. (**a**) Structural behavior of CSCL in elastoplastic stage; (**b**) Structural behavior of CSIL layer in elastoplastic stage.

The displacement in the plastic zone of the CSCL can be obtained by Eq. (5).

$$u_{sc} = \frac{(1+v_2)(1-2v_2)Ccot\varphi}{E_2}\left[1-\left(1+\frac{P_1}{Ccot\varphi}\right)\left(\frac{r}{r_2}\right)^{B-1}\right]r+\frac{K}{r} \tag{5}$$

When $r = r_{sc}$, the displacement at the outer boundary of the plastic zone in the CSCL can be determined by Eq. (6).

$$u_{scpo} = \frac{(1+v_2)(1-2v_2)Ccot\varphi}{E_2}\left[1-\left(1+\frac{P_1}{Ccot\varphi}\right)\left(\frac{r_{sc}}{r_2}\right)^{B-1}\right]r_{sc}+\frac{K}{r_{sc}} \tag{6}$$

where σ_{rscp} is the radial stress in plastic zone of CSCL, MPa; $\sigma_{\theta scp}$ is the circumferential stress in plastic zone of CSCL, MPa; C is the cohesion of CSCL, GPa; P_{sc} is the interface contact stress at elastoplastic boundary, MPa; φ is the internal friction angle of CSCL, °; r_{sc} is the radius of elastoplastic boundary, mm; E_2 is the elastic modulus of CSCL, GPa; v_2 is the poisson's ratio of CSCL, dimensionless; u_{sc} is the displacement of CSCL, mm; u_{scpo} is the displacement at outer boundary of plastic zone, mm; K is the integration constant, dimensionless; N is the coefficient, $N = \frac{1-sin\varphi}{1+sin\varphi}$.

(2) Elastic zone in the CSCL.

According to the Lamé formula, the stresses in the CSCL at the elastoplastic boundary can be obtained by Eq. (7) .

$$\begin{cases} \sigma_{rsce} = \frac{r_3^2(P_2-P_{sc})}{r_3^2-r_{sc}^2}+\frac{r_{sc}^2P_{sc}-r_3^2P_2}{r_3^2-r_{sc}^2} \\ \sigma_{\theta sce} = -\frac{r_3^2(P_2-P_{sc})}{r_3^2-r_{sc}^2}+\frac{r_{sc}^2P_{sc}-r_3^2P_2}{r_3^2-r_{sc}^2} \end{cases} \tag{7}$$

When $r = r_{sc}$, Simultaneously solving the Mohr–Coulomb criterion and Eq. (8) yields.

$$P_2 = \frac{1}{r_3^2(1+sin\varphi)}\left[\left(r_3^2+r_{sc}^2sin\varphi\right)P_{sc}-\left(r_3^2-r_{sc}^2\right)Ccos\varphi\right] \tag{8}$$

The displacements at the inner and outer walls of the elastic zone in the CSCL can be determined by Eq. (9) and Eq. (10).

$$u_{sceo} = \frac{1+v_2}{E_2}\frac{2(1-v_2)r_{sc}^2r_3}{r_3^2-r_{sc}^2}P_{sc}-\frac{1+v_2}{E_2}\frac{r_{sc}^2r_3+(1-2v_2)r_3^3}{r_3^2-r_{sc}^2}P_2 \tag{9}$$

$$u_{scei} = \frac{1+v_2}{E_2}\frac{r_{sc}r_3^2+(1-2v_2)r_{sc}^3}{r_3^2-r_{sc}^2}P_{sc}-\frac{1+v_2}{E_2}\frac{2(1-v_2)r_{sc}r_3^2}{r_3^2-r_{sc}^2}P_2 \tag{10}$$

By utilizing the displacement continuity condition at the elastoplastic boundary of the CSCL $u_{scei} = u_{scpo}$, solving Eq. (11) yields the solution.

$$K = \frac{2\left(1-v_2^2\right)r_{sc}^2sin\varphi}{E_2(1+sin\varphi)}(P_{sc}+Ccot\varphi) \tag{11}$$

When the displacement at the inner wall of the plastic zone in the CSCL region can be determined by Eq. (12).

$$u_{scpi} = \left[\frac{2(1-v_2^2)r_{sc}^2 sin\varphi}{E_2(1+sin\varphi)r_2}\left(\frac{r_{sc}}{r_2}\right)^{N-1} - \frac{(1+v_2)(1-2v_2)r_2}{E_2}\right]P_1 + \frac{2(1-v_2^2)r_{sc}^2 sin\varphi}{E_2(1+sin\varphi)r_2}\left(\frac{r_{sc}}{r_2}\right)^{N-1} Ccot\varphi \quad (12)$$

where σ_{rsce} is the radial stress in elastic zone of CSCL, MPa; $\sigma_{\theta sce}$ is the circumferential stress in elastic zone of CSCL, MPa; P_2 is the interface contact stress at outer boundary of elastic zone in CSCL, MPa; r_3 is the outer boundary radius of elastic zone in CSCL, mm; u_{sceo} is the displacement at outer boundary of elastic zone in CSCL, mm; u_{scei} is the displacement at inner boundary of elastic zone in CSCL, mm; u_{scpi} is the displacement at inner boundary of plastic zone in CSCL, mm.

Fully plastic state of the CSCL

When the CSCL enters the fully plastic state (i.e., no elastic zone remains), the elastoplastic boundary radius of the CSCL is $r_{sc} \geq r_3$.

The displacement at the inner boundary of the CSCL in the fully plastic state can be determined by Eq. (13).

$$u_{scpi} = -\frac{(1+v_2)(1-2v_2)}{E_2}P_1 r_2 + \frac{K}{r_2} \quad (13)$$

Under internal pressure loading, the displacement of the inner wall of the CSCL equals the displacement of the outer boundary of the casing according to the displacement boundary condition, K can be determined.

$$u_{scpi} = u_{co} \quad (14)$$

$$K = S_1 P_i r_2 + \left[\frac{(1+v_2)(1-2v_2)}{E_2}r_2 - S_2\right] P_1 r_2 \quad (15)$$

Substituting Eq. (15) into Eq. (16) yields the displacement expression for the plastic zone of the fully plastic CSCL.

$$u_{scp} = \frac{(1+v_2)(1-2v_2)Ccot\varphi}{E_2}\left[1 - \left(1 + \frac{P_1}{Ccot\varphi}\right)\left(\frac{r}{r_2}\right)^{N-1}\right] r + S_1 P_i \frac{r_2}{r} + \left[\frac{(1+v_2)(1-2v_2)}{E_2}r_2 - S_2\right] P_1 \frac{r_2}{r} \quad (16)$$

The stress expression for the CSCL in the fully plastic stage differs from that in the elastoplastic stage. When $r = r_3$, $\sigma_r|_{r=r_3} = -P_2$, P_2 can be determined.

$$P_2 = Ccot\varphi\left[\left(1 + \frac{P_1}{Ccot\varphi}\right)\left(\frac{r_3}{r_2}\right)^{N-1} - 1\right] \quad (17)$$

where u_{scp} is the displacement in the Fully Plastic Zone of CSCL, mm.

Stress and displacement of the CSIL during CO_2 injection

This study focuses on the sealing integrity of the cement sheath in long-term CO_2 storage wells. During the initial stage of CO_2 intrusion, the formation of calcium carbonate leads to a reduction in porosity and permeability of the cement, along with an increase in mechanical strength. However, over time, the dissolution of calcium carbonate results in an increase in porosity and permeability, accompanied by a significant decrease in mechanical strength. During the internal pressure loading phase in the later stage of storage, the CSIL exhibits superior mechanical strength and properties compared to the CSCL. Specifically, the CSCL enters the elastoplastic stage earlier than the CSIL. While the CSCL is in the elastoplastic stage, the CSIL remains in the elastic stage. Only after the CSCL enters the fully plastic stage does the CSIL have the potential to undergo plastic deformation.

Taking the fully elastic state of the CSIL during the CO_2 injection and internal pressure loading phase as an example, its displacement and stress responses are analyzed. The analytical methods for stress and displacement in the elastoplastic and fully plastic stages of the CSIL are consistent with those applied to the CSCL.

The stress distribution at each point of the CSIL can be determined by Eq. (18).

$$\begin{cases} \sigma_{rsn} = \frac{r_3^2 r_4^2 (P_3 - P_2)}{r_4^2 - r_3^2}\frac{1}{r^2} + \frac{r_3^2 P_2 - r_4^2 P_3}{r_4^2 - r_3^2} \\ \sigma_{\theta sn} = -\frac{r_3^2 r_4^2 (P_3 - P_2)}{r_4^2 - r_3^2}\frac{1}{r^2} + \frac{r_3^2 P_2 - r_4^2 P_3}{r_4^2 - r_3^2} \end{cases} \quad (18)$$

where σ_{rsn} is the radial stress of CSIL, MPa; $\sigma_{\theta sn}$ is the circumferential stress of CSIL, MPa; P_3 is the interface contact stress at outer boundary of CSIL, MPa; r_4 is the outer radius of elastic zone in CSIL, mm.

The radial displacement of the inner wall of the CSIL can be determined by Eq. (19).

$$\begin{aligned} u_{sni} &= \frac{1+v_3}{E_3}\frac{r_3 r_4^2 + (1-2v_3)r_3^3}{r_4^2 - r_3^2}P_2 - \frac{1+v_3}{E_3}\frac{2(1-v_3)r_3 r_4^2}{r_4^2 - r_3^2}P_3 \\ &= S_3 P_2 - S_4 P_3 \end{aligned} \quad (19)$$

where u_{sni} is the radial displacement at the inner boundary of CSIL, mm; v_3 is the poisson's ratio of formation, dimensionless; E_3 is the elastic modulus of formation, GPa; S_3 and S_4 are coefficients in formation radial displacement formula, dimensionless.

The radial displacement of the outer wall of the CSIL can be determined by Eq. (20).

$$\begin{aligned} u_{sno} &= \frac{1+v_3}{E_3}\frac{2(1-v_3)r_3^2 r_4}{r_4^2-r_3^2}P_2 - \frac{1+v_3}{E_3}\frac{r_3^2 r_4+(1-2v_3)r_4^3}{r_4^2-r_3^2}P_3 \\ &= S_5 P_2 - S_6 P_3 \end{aligned} \tag{20}$$

where u_{sno} is the radial displacement at the outer boundary of CSIL, mm; S_5 and S_6 are coefficients in formation radial displacement formula, dimensionless.

Stress and displacement of the formation during CO_2 injection

The stress distribution at any point in the surrounding rock formation can be derived from Lame's equations, as given by Eq. (21).

$$\begin{cases} \sigma_{rf} = \frac{r_4^2 r_5^2 (P_o - P_3)}{r_5^2 - r_4^2}\frac{1}{r^2} + \frac{r_4^2 P_3 - r_5^2 P_o}{r_5^2 - r_4^2} \\ \sigma_{\theta f} = -\frac{r_4^2 r_5^2 (P_0 - P_3)}{r_5^2 - r_4^2}\frac{1}{r^2} + \frac{r_4^2 P_3 - r_5^2 P_o}{r_5^2 - r_4^2} \end{cases} \tag{21}$$

The radial displacement of the inner wall in the surrounding rock formation can be determined by Eq. (22).

$$\begin{aligned} u_{fi} &= \frac{1+v_4}{E_4}\frac{r_4 r_5^2+(1-2v_4)r_4^3}{r_5^2-r_4^2}P_3 - \frac{1+v_4}{E_4}\frac{2(1-v_4)r_4 r_5^2}{r_5^2-r_4^2}P_o \\ &= S_{11}P_3 - S_{12}P_o \end{aligned} \tag{22}$$

where σ_{rf} is the radial stress of surrounding rock formation, MPa; $\sigma_{\theta f}$ is the circumferential stress of surrounding rock formation, MPa; P_o is the formation confinement stress, MPa; r_5 is the radius of surrounding rock formation, mm; u_{fi} is the radial displacement of surrounding rock formation, mm; v_4 is the poisson's ratio of formation, dimensionless; E_4 is the elastic modulus of formation, GPa ; S_7 and S_8 are coefficients in formation radial displacement formula, dimensionless.

During the CO_2 injection and internal pressure loading phase, the mechanical model of the casing-CSCL-CSIL-formation assembly satisfies the continuous radial displacement condition. Based on Working Condition 1, where the CSCL enters the elastoplastic stage while the CSIL remains fully elastic, a system of Eqs. (23) can be derived by combining these conditions. The above equations form a system of six equations with unknowns $P_1, P_2, P_3, P_{sc}, r_{sc}$ and K. Given the CO_2 injection internal pressure and the formation confining pressure, this system of equations can be solved.

$$\begin{cases} u_{co} = u_{scpi} \\ u_{scpo} = u_{scei} \\ u_{sceo} = u_{sni} \\ u_{sno} = u_{fi} \\ P_2 = \frac{1}{r_3^2(1+\sin\varphi)}\left[\left(r_3^2 + r_{sc}^2\sin\varphi\right)P_{sc} - \left(r_3^2 - r_{sc}^2\right)C\cos\varphi\right] \\ K = \frac{2\left(1-v_2^2\right)r_{sc}^2\sin\varphi}{E_2(1+\sin\varphi)}\left(P_{sc} + C\cot\varphi\right) \end{cases} \tag{23}$$

Based on Working Condition 2, where the CSCL enters the fully plastic stage while the CSIL remains fully elastic, a system of Eqs. (24) can be derived by combining these conditions. The above equations form a system of five equations with unknowns P_1、P_2、P_3、r_{sc} and K. Given the CO_2 injection internal pressure and the formation confining pressure, this system of equations can be solved.

$$\begin{cases} u_{co} = u_{scpi} \\ u_{scpo} = u_{sni} \\ u_{sno} = u_{fi} \\ P_2 = \frac{1}{r_3^2(1+\sin\varphi)}\left[\left(r_3^2 + r_{sc}^2\sin\varphi\right)P_{sc} - \left(r_3^2 - r_{sc}^2\right)C\cos\varphi\right] \\ K = \frac{2\left(1-v_2^2\right)r_{sc}^2\sin\varphi}{E_2(1+\sin\varphi)}\left(P_{sc} + C\cot\varphi\right) \end{cases} \tag{24}$$

Stress and displacement of the CSCL during CO_2 storage

At the initial storage stage, the casing internal pressure at this stage equals the pressure at the end of the loading phase; the subscript b denotes the initial storage stage (i.e., the final stage of the loading state), and j denotes the final storage stage (i.e., the initial stage of the unloading state). During the casing internal pressure unloading phase, the cement sheath is treated as an ideal plastic material. This implies that the elastic strain component recovers upon unloading, with stress variations obeying Hooke's law. Conversely, the plastic strain component manifests as permanent deformation after unloading.

Plastic zone of the CSCL

For the plastic zone in the CSCL, the radial displacement at the inner wall of the plastic zone is the sum of the displacement induced during the CO_2 injection phase and the deformation at the inner wall during unloading.

$$u_{scpij} = u_{scpib} + u_{scpih} \tag{25}$$

where u_{scpij} is the radial displacement at the inner wall of the plastic zone in the CSCL, mm; u_{scpib} is the displacement at the inner wall induced during the CO_2 injection phase, mm; u_{scpih} is the displacement at the inner wall generated during the unloading phase, mm.

In this equation, the displacement at the inner wall of the plastic zone in the CSCL during the CO_2 injection phase can be derived from the mechanical model of the loading phase. Specifically, it corresponds to the displacement when the casing internal pressure is loaded to the design pressure for CO_2 injection. Based on the assumption that the cement sheath exhibits ideal elastoplastic behavior during the unloading phase, the displacement variation at the inner wall of the plastic zone induced by unloading can be determined.

$$u_{scpih} = \frac{1+v_2}{E_2}\frac{r_2 r_{sc}^2+(1-2v_2)r_2^3}{r_{sc}^2-r_2^2}\Delta P_1 - \frac{1+v_2}{E_2}\frac{2(1-v_2)r_2 r_{sc}^2}{r_{sc}^2-r_2^2}\Delta P_{sc} \tag{26}$$

where ΔP_1 is the stress variation at the inner wall of the plastic zone in the CSCL, MPa; ΔP_{sc} is the stress variation at the outer boundary of the plastic zone (i.e., the interface between the plastic and elastic regions) in the CSCL, MPa.

$$\begin{cases} \Delta P_1 = P_{1j} - P_{1b} \\ \Delta P_{sc} = P_{scj} - P_{scb} \end{cases} \tag{27}$$

Similarly, the radial displacement at the outer wall of the plastic zone in the CSCL during the final stage of unloading is

$$u_{scpoj} = u_{scpob} + u_{scpoh} \tag{28}$$

where u_{scpoj} is the radial displacement at the outer wall of the plastic zone in the CSCL, mm; u_{scpob} is the displacement at the outer wall induced during the CO_2 injection phase, mm; u_{scpoh} is the displacement at the outer wall generated during the unloading phase, mm.

The deformation at the outer wall of the CSCL during the unloading phase can be determined by Eq. (29).

$$u_{scpoh} = \frac{1+v_2}{E_2}\frac{2(1-v_2)r_2^2 r_{sc}}{r_{sc}^2-r_2^2}(P_{1j}-P_{1b}) - \frac{1+v_2}{E_2}\frac{r_2^2 r_{sc}+(1-2v_2)r_{sc}^3}{r_{sc}^2-r_2^2}(P_{scj}-P_{scb}) \tag{29}$$

Elastic zone of the CSCL

During the final stage of unloading, the radial displacement at the inner wall of the elastic zone in the CSCL can be determined by Eq. (30).

$$u_{sceij} = \frac{1+v_2}{E_2}\frac{r_{sc} r_3^2+(1-2v_2)r_{sc}^3}{r_3^2-r_{sc}^2}P_{scj} - \frac{1+v_2}{E_2}\frac{2(1-v_2)r_{sc} r_3^2}{r_3^2-r_{sc}^2}P_{2j} \tag{30}$$

where u_{sceij} is the radial displacement at the inner wall of the elastic zone in the CSCL, mm; P_{scj} is the stress at the inner wall of the elastic zone in the CSCL, MPa; P_{2j} is the stress at the outer wall of the elastic zone in the CSCL, MPa.

The radial displacement at the outer wall of the elastic zone in the CSCL during the final stage of unloading can be determined by Eq. (31).

$$u_{sceoj} = \frac{1+v_2}{E_2}\frac{2(1-v_2)r_{sc}^2 r_3}{r_3^2-r_{sc}^2}P_{scj} - \frac{1+v_2}{E_2}\frac{r_{sc}^2 r_3+(1-2v_2)r_3^3}{r_3^2-r_{sc}^2}P_{2j} \tag{31}$$

where u_{sceoj} is the radial displacement at the outer wall of the elastic zone in the CSCL, mm.

During the unloading phase under this working condition, the casing, CSIL, and formation surrounding rock remain elastic throughout. The analysis of their stress and displacement follows a method similar to that used during the injection phase and will not be reiterated here.

During the unloading process, since the casing remains elastic while the CSCL undergoes plastic deformation, a micro-annulus will form at the primary cementing interface when the interfacial contact force at the inner wall of the CSCL exceeds the interfacial bonding capacity. Prior to the appearance of the micro-annulus, the mechanical model still satisfies the continuous radial displacement condition, and a system of Eqs. (32) can be derived by combining these conditions.

$$\begin{cases} u_{coj} = u_{scpij} \\ u_{scpoj} = u_{sceij} \\ u_{sceoj} = u_{snij} \\ u_{snoj} = u_{fij} \end{cases} \tag{32}$$

where u_{coj} is radial displacement of casing outer wall during unloading phase, mm; u_{snij} is the radial displacement of inner wall of CSIL during unloading phase, mm; u_{snoj} is the radial displacement of outer wall of CSIL during unloading phase, mm; u_{fij} is the radial displacement of formation inner wall during unloading phase, mm.

The above expression represents a system of four equations with unknowns P_{1j}, P_{scj}, P_{2j} and P_{3j}. By solving for the interfacial contact forces P_{1j}, P_{scj}, P_{2j} and P_{3j}, the stress and displacement values at each point of the casing-CSCL-CSIL-formation assembly can be determined.

Micro-annulus calculation at the primary cementing interface

During CO_2 injection and storage, when the casing internal pressure is unloaded, the interfacial contact force at the boundary between the inner wall of the CSCL and the outer wall of the casing transitions into tensile stress. When this tensile stress exceeds the cementing bond strength of the primary interface, separation occurs between

the inner wall of the CSCL and the outer wall of the casing, resulting in the formation of a micro-annulus at the primary cementing interface. Once the micro-annulus is generated, no contact force exists between the inner wall of the CSCL and the outer wall of the casing. At this point, the entire model can be divided into two parts: the casing, and the cement sheath-formation system containing the corroded layer.

Depending on the casing internal pressure during CO_2 injection, the cement sheath may exhibit either an elastoplastic stage or a fully plastic stage during pressure unloading, and the mechanical models for these two scenarios differ. Here, taking the working condition where the CSCL enters the elastoplastic stage while the CSIL remains fully elastic as an example, the calculation method for the micro-annulus at the primary cementing interface is introduced.

Radial displacement of the casing

After the micro-annulus is generated at the primary cementing interface, the casing internal pressure during injection and storage cannot be transmitted to the cement sheath and formation. At this point, the casing is only subjected to the unloaded internal pressure, and the radial displacement at the outer wall of the casing can be determined by Eq. (33).

$$u_{coj} = \frac{1+v_1}{E_1}\frac{2(1-v_1)r_1^2 r_2}{r_2^2-r_1^2}P_{ij} \tag{33}$$

where u_{coj} is the radial displacement at the outer wall of the casing, mm; P_{ij} is the unloaded internal pressure, MPa.

Radial displacement of the plastic zone in the CSCL

After the interface between the inner wall of the CSCL and the outer wall of the casing becomes detached, the plastic zone of the CSCL is subjected to the interfacial contact force at the outer boundary of the plastic zone. The radial displacement at the inner wall of the plastic zone in the CSCL is equal to the displacement generated during the internal pressure loading phase plus the deformation at the inner wall of the plastic zone during unloading. This can be determined by Eq. (34).

$$u_{scpij} = u_{scpib} + u_{scpih} \tag{34}$$

The displacement generated during the internal pressure loading phase in this equation can be derived from the mechanical model of the loading phase, specifically corresponding to the displacement at the inner wall of the plastic zone in the CSCL when the casing internal pressure is loaded to the design injection pressure for CO_2. Based on the assumption that the cement sheath exhibits ideal elastoplastic behavior during the unloading phase, the variation at the inner wall induced by unloading can be determined using Eq. (35).

$$u_{scpih} = \frac{1+v_2}{E_2}\frac{r_2 r_{sc}^2+(1-2v_2)r_2^3}{r_{sc}^2-r_2^2}\Delta P_1 - \frac{1+v_2}{E_2}\frac{2(1-v_2)r_2 r_{sc}^2}{r_{sc}^2-r_2^2}\Delta P_{sc} \tag{35}$$

The solutions for ΔP_1 and ΔP_{sc} are determined by Eq. (27). In the Eq. (29), $P_{1j} = 0$. Therefore, Eq. (35) can be rewritten as Eq. (36).

$$u_{scpih} = \frac{1+v_2}{E_2}\frac{r_2 r_{sc}^2+(1-2v_2)r_2^3}{r_{sc}^2-r_2^2}(-P_{1b}) - \frac{1+v_2}{E_2}\frac{2(1-v_2)r_2 r_{sc}^2}{r_{sc}^2-r_2^2}(P_{scj}-P_{scb}) \tag{36}$$

Similarly, after the micro-annulus appears at the primary interface, the radial displacement at the outer wall of the plastic zone in the CSCL can be determined by Eq. (37).

$$u_{scpoj} = u_{scpob} + \frac{1+v_2}{E_2}\frac{2(1-v_2)r_2^2 r_{sc}}{r_{sc}^2-r_2^2}(-P_{1b}) - \frac{1+v_2}{E_2}\frac{r_2^2 r_{sc}+(1-2v_2)r_{sc}^3}{r_{sc}^2-r_2^2}(P_{scj}-P_{scb}) \tag{37}$$

Radial displacement of the elastic zone in the CSCL

During the final stage of internal pressure unloading, both the inner and outer walls of the elastic zone in the CSCL are subjected to forces. The radial displacement of the inner wall of the elastic zone in the CSCL can be determined by Eq. (38).

$$u_{sceij} = \frac{1+v_2}{E_2}\frac{r_{sc}r_3^2+(1-2v_2)r_{sc}^3}{r_3^2-r_{sc}^2}P_{scj} - \frac{1+v_2}{E_2}\frac{2(1-v_2)r_{sc}r_3^2}{r_3^2-r_{sc}^2}P_{2j} \tag{38}$$

The radial displacement of the outer wall of the elastic zone in the CSCL can be determined by Eq. (39).

$$u_{sceoj} = \frac{1+v_2}{E_2}\frac{2(1-v_2)r_{sc}^2 r_3}{r_3^2-r_{sc}^2}P_{scj} - \frac{1+v_2}{E_2}\frac{r_{sc}^2 r_3+(1-2v_2)r_3^3}{r_3^2-r_{sc}^2}P_{2j} \tag{39}$$

Radial displacement of the CSIL

During the final stage of internal pressure unloading, both the inner and outer walls of the CSIL are subjected to forces. The radial displacement of the inner wall of the CSIL can be determined by Eq. (40).

$$u_{snij} = \frac{1+v_3}{E_3}\frac{r_3 r_4^2+(1-2v_3)r_3^3}{r_4^2-r_3^2}P_{2j} - \frac{1+v_3}{E_3}\frac{2(1-v_3)r_3 r_4^2}{r_4^2-r_3^2}P_{3j} \tag{40}$$

where u_{snij} is radial displacement of the inner wall of the CSIL, mm.

The radial displacement of the outer wall of the CSIL can be determined by Eq. (41).

$$u_{snoj} = \frac{1+v_3}{E_3}\frac{2(1-v_3)r_3^2 r_4}{r_4^2-r_3^2}P_{2j} - \frac{1+v_3}{E_3}\frac{r_3^2 r_4+(1-2v_3)r_4^3}{r_4^2-r_3^2}P_{3j} \tag{41}$$

where u_{snoj} is radial displacement of the outer wall of the CSIL, mm.

Radial displacement of the formation

After the micro-annulus appears at the primary cementing interface, both the inner and outer walls of the formation surrounding rock are subjected to forces. The radial displacement of the inner wall of the formation can be determined by Eq. (42).

$$u_{fij} = \frac{1+v_4}{E_4}\frac{r_4 r_5^2+(1-2v_4)r_4^3}{r_5^2-r_4^2}P_{3j} - \frac{1+v_4}{E_4}\frac{2(1-v_4)r_4 r_5^2}{r_5^2-r_4^2}P_o \tag{42}$$

After the micro-annulus appears at the primary interface, the CCS remains tightly bonded to the formation, satisfying the continuous displacement condition. By combining the above equations, a system of Eqs. (43) can be derived. This system consists of three equations, and solving it yields the three interfacial contact pressures P_{scj} and P_{2j} and P_{3j}. Substituting these solved interfacial contact forces into the equations allows for the determination of the radial displacement at the inner wall of the CSCL.

$$\begin{cases} u_{scpoj} = u_{sceij} \\ u_{sceoj} = u_{snij} \\ u_{snoj} = u_{fij} \end{cases} \tag{43}$$

The aperture size of the micro-annulus at the primary cementing interface can be calculated from the displacement of the casing outer wall and the displacement of the inner wall of the CSCL, as determined by Eq. (44).

$$\begin{cases} W_j = (r_2 + u_{scpij}) - (r_2 + u_{coj}) \\ W_j = u_{scpij} - u_{coj} \end{cases} \tag{44}$$

Results

The geometric dimensions of the theoretical solution model were referenced to the wellbore structure of a CO_2 injection well in a Chinese oilfield, with specific parameters detailed in Table 1. The outer diameter of the stratum surrounding rock was set to ten times that of the cement sheath based on Saint–Venant's principle, which effectively eliminates boundary effects on stress field distribution. The mechanical property parameters of the cement sheath before and after CO_2 corrosion refer to the data in Ref.[27]. The solution of this mechanical model is implemented through MATLAB software.

Parameters	Value
Outer diameter of casing/mm	139.7
Wall thickness of casing/mm	15.44
Outer diameter of cement sheath/mm	251.5
Thickness of CSCL/mm	5
Outer diameter of formation/mm	2515
Elastic modulus of casing/GPa	206
Poisson's ratio of casing	0.29
Elastic modulus of cement sheath/GPa	5.8256
Poisson's ratio of cement sheath	0.159
Cohesion of cement sheath/MPa	11.2
Friction angle of cement sheath/°	27.4
Elastic modulus of CSCL/GPa	9.2487
Poisson's ratio of CSCL	0.167
Cohesion of CSCL/MPa	12.390
Friction angle of CSCL/°	4.27
Elastic modulus of formation/GPa	26.133
Poisson's ratio of formation	0.224
Cohesion of formation/MPa	16
Friction angle of formation/°	36
Bonding strength at casing-cement interface/MPa	0

Table 1. Materials and Dimensional Parameters of CCUS Wellbore Assembly Components.

The mechanical parameters of the intact cement sheath and the CSCL listed in Table 1 are taken from Ref.27, who performed triaxial tests on Class G cement specimens before and after CO_2 exposure under geological storage conditions. Specifically, the intact cement properties correspond to uncorroded specimens after standard curing, whereas the CSCL parameters are obtained from specimens with an approximately 5 mm CO_2-corroded layer after exposure for 60 days at 20 MPa and 60 °C. Formation and casing mechanical parameters are adopted from typical field data of the studied CO_2 injection well.

Model verification

To verify the correctness of the proposed elastoplastic analytical model and its numerical implementation, the thickness of the CSCL was first set to zero. Under this condition, the casing-CSCL-CSIL-formation assembly degenerates into the conventional three-layer casing–cement sheath–formation system, and the governing equations reduce to the classical elastoplastic formulations for wellbore assemblies reported in the literature.

For this degenerated configuration, we adopted the same geometric dimensions, mechanical parameters and in-situ stress conditions as those used by Chu et al.[17] The radial contact stresses at the primary interface (between casing and cement sheath) and the secondary interface (between cement sheath and formation) were calculated for different internal casing pressures. The results were then compared with the interface stresses reported in Ref[17].

As shown in Fig. 3, the radial contact stresses at both the primary and secondary interfaces predicted by the present model exhibit an excellent agreement with the results of Ref[17] over the entire internal pressure range. The two sets of curves almost coincide, and the maximum relative deviation is less than 2.4%. This demonstrates that, in the absence of a corroded layer, the proposed model correctly degenerates to the conventional casing–cement sheath–formation elastoplastic solutions, thereby validating both the analytical derivation and the MATLAB implementation. On this basis, the extended casing-CCS-formation model incorporating a corroded cement sheath layer can be regarded as reliable for subsequent analyses of CO_2 corrosion–stress coupling effects on cement sheath integrity.

Integrity analysis of cement sheath

Taking the base case in Table 1 as an example, this study analyzes the stress and displacement responses of both corroded and uncorroded cement sheaths under 60 MPa injection pressure loading and unloading conditions. The radial stress nephograms of both cement sheaths at the end of the loading phase are shown in Fig. 4, while the comparative radial stress distributions along the radius are presented in Fig. 5. As observed in Fig. 4, when the injection pressure reaches 60 MPa, both the uncorroded and corroded cement sheaths experience compressive radial stresses, with the maximum compressive stress occurring at the primary cementing interface, indicating that this interface is the critical zone during injection. Due to the presence of a 5 mm corroded region with weakened mechanical properties, the CCS exhibits significantly higher radial stress values at the same radial distance from the wellbore center compared to the uncorroded cement sheath. This demonstrates that under CO_2 injection conditions, the CCS is more prone to irreversible plastic deformation under higher radial compressive stresses. During the unloading phase, the interfacial contact stress at the primary cementing interface transitions from compressive to tensile. When this tensile stress exceeds the interfacial bonding strength, a micro-annulus forms. Calculations reveal that after unloading from 60 MPa, the CCS with a 5 mm corroded layer develops a micro-annulus with an aperture of 0.0519 mm, while the uncorroded cement

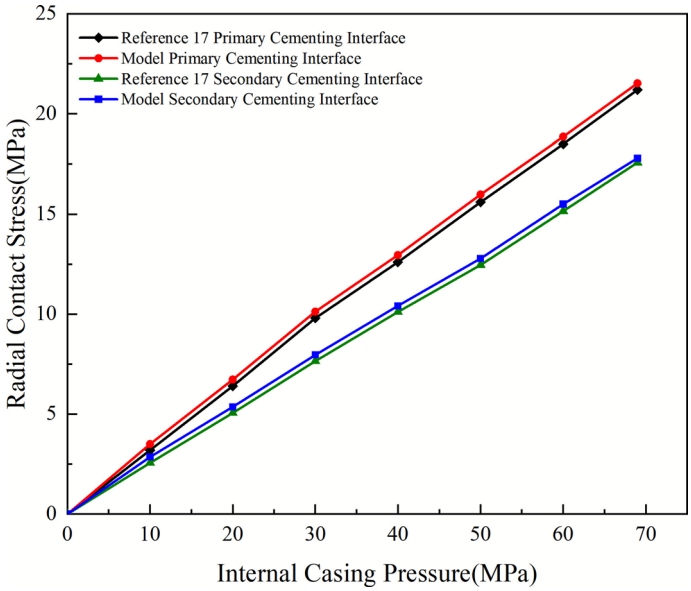

Fig. 3. Comparison of radial contact stresses at the primary and secondary interfaces between the present model and Ref.[17].

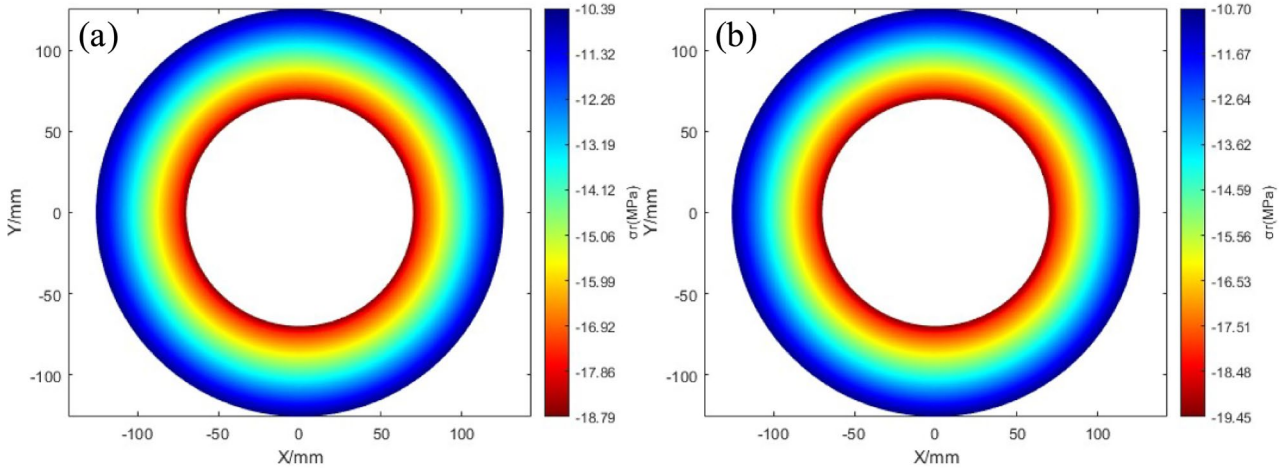

Fig. 4. (**a**) Radial stress nephogram of the uncorroded cement sheath when the injection pressure is loaded to 60 MPa; (**b**) Radial stress nephogram of the CCS when the injection pressure is loaded to 60 MPa.

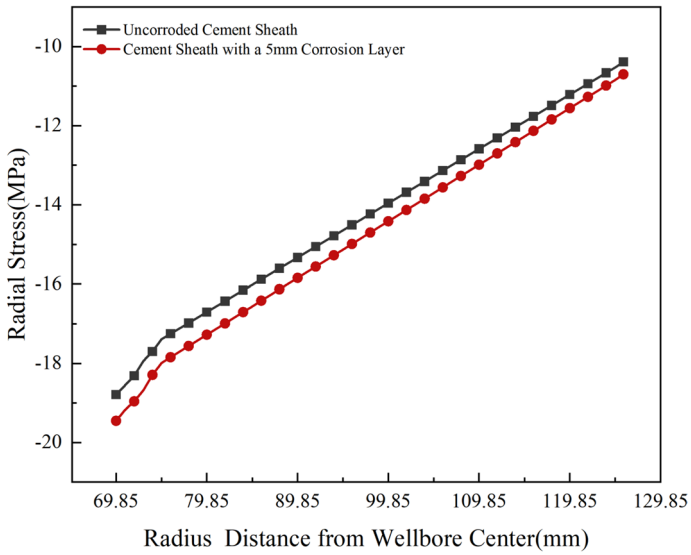

Fig. 5. Radial stress distribution along the radius of the cement sheath.

sheath exhibits a smaller aperture of 0.0238 mm. This confirms that CO_2-induced corrosion causes significant mechanical degradation in the cement sheath, leading to greater plastic deformation under the same injection pressure compared to uncorroded cement. Furthermore, these results emphasize that under long-term storage conditions, CCS are more susceptible to sealing integrity failure.

As can be seen in Fig. 4, for both the intact sheath and the CCS, the region adjacent to the casing is subjected to the highest compressive radial stress and preferentially enters the plastic state, while the outer part of the sheath remains elastic. The plastic zone in the CCS extends over a larger radial distance than in the intact cement, reflecting the weaker mechanical resistance of the corroded layer. Correspondingly, Fig. 5 shows that the radial stress in the CCS decays more steeply from the casing side towards the formation, and the contact stress at the primary interface is significantly more compressive than in the intact case under the same injection pressure. This broader plastic zone and higher compressive stress explain why the CCS undergoes larger residual deformation and develops a wider micro-annulus upon unloading.

Effects of injection pressures on corroded cement sheath

Different injection pressures were set to 40, 50, 60, 70, 80, and 100 MPa, with CSCL thickness of 5 mm in the cement sheath. Other calculation parameters were configured according to the base case in Table 1. The radial stress of the cement sheath at the end of loading and the micro-annulus aperture after unloading under different injection pressures were calculated. Figure 6 shows the nephogram of radial stress in the cement sheath at the end of loading under different injection pressures, and the specific calculation results are presented in Figs. 7 and 8. As shown in Fig. 7, higher injection pressures result in greater radial stress in the corroded cement sheath

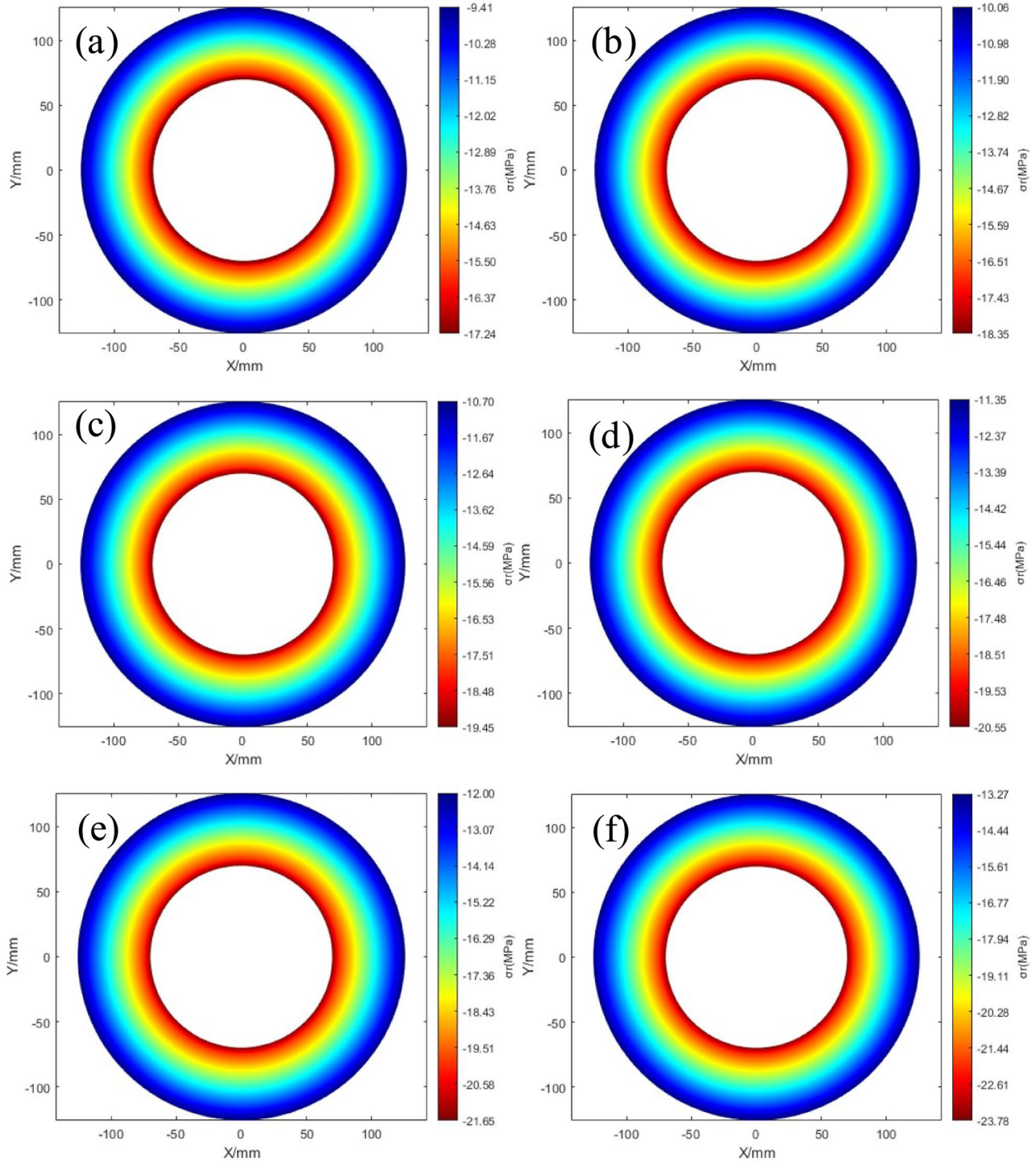

Fig. 6. (**a**) Radial stress nephogram of CCS under 40 MPa injection pressure; (**b**) Radial stress nephogram of CCS under 50 MPa injection pressure; (**c**) Radial stress nephogram of CCS under 60 MPa injection pressure; (**d**) Radial stress nephogram of CCS under 70 MPa injection pressure; (**e**) Radial stress nephogram of CCS under 80 MPa injection pressure; (**b**) Radial stress nephogram of CCS under 100 MPa injection pressure.

at the end of loading, with the maximum stress occurring at the primary cementing interface. Figure 8 indicates that the micro-annulus aperture at the primary interface of the CCS also increases with rising injection pressure. At an injection pressure of 40 MPa, the micro-annulus aperture is 0.0211 mm, while it increases to 0.1113 mm when the injection pressure reaches 100 MPa. Under such conditions, CO_2 is highly prone to leakage through the micro-annulus at the primary interface, leading to failure in CO_2 injection and storage. This demonstrates that higher injection pressures cause increased plastic deformation in the cement sheath. Therefore, during field

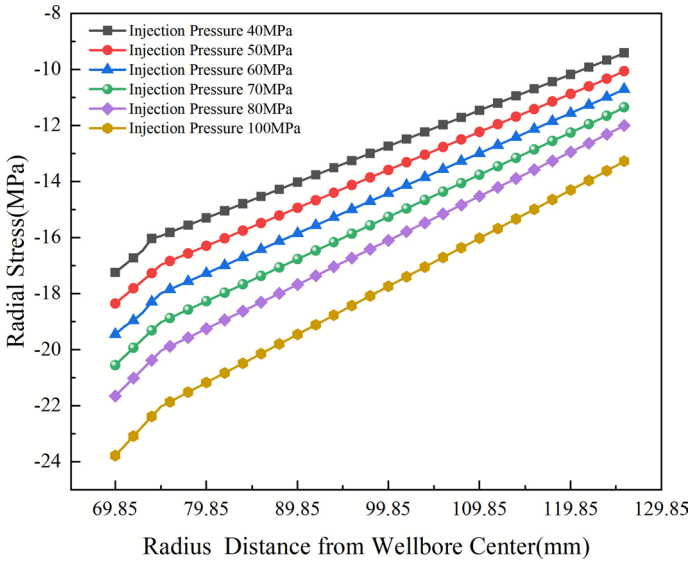

Fig. 7. Effects of differential injection pressures on cement sheath radial stress.

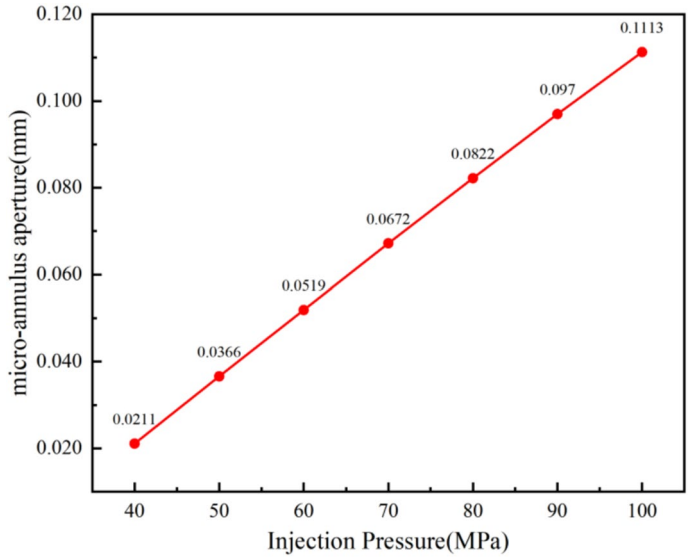

Fig. 8. Micro-annulus at primary cementing interface under differential injection pressures.

operations for CO_2 injection into wellbores, appropriate injection pressures should be rationally selected to ensure the sealing integrity of the cement sheath.

Effect of CSCL thickness on corroded cement sheath

Different CSCL thicknesses of the cement sheath were set to 5, 10, 15, 20, 25, and 30 mm, with an injection pressure of 60 MPa. Other calculation parameters were configured according to the base case in Table 1. The radial stress of the cement sheath at the end of loading and the micro-annulus aperture after unloading under different CSCL thicknesses were calculated. Figure 9 shows the nephogram of radial stress in the cement sheath at the end of loading under different CSCL thicknesses, and the specific calculation results are presented in Figs. 10 and 11. As shown in Fig. 10, as the CSCL thickness increases, the radial stress experienced by the cement sheath at the end of internal pressure loading increases, raising the risk of plastic deformation in the cement sheath. As illustrated in Fig. 11, when the CSCL thickness increases from 5 to 30 mm, the micro-annulus aperture at the primary cementing interface increases from 0.0519 mm to 0.0579 mm, representing a growth of 11.5%. This indicates that the influence of CSCL thickness on the micro-annulus aperture is relatively limited. Although an increase in CSCL thickness leads to a larger micro-annulus aperture at the primary interface, its impact is less significant compared to the changes induced by higher injection pressures.

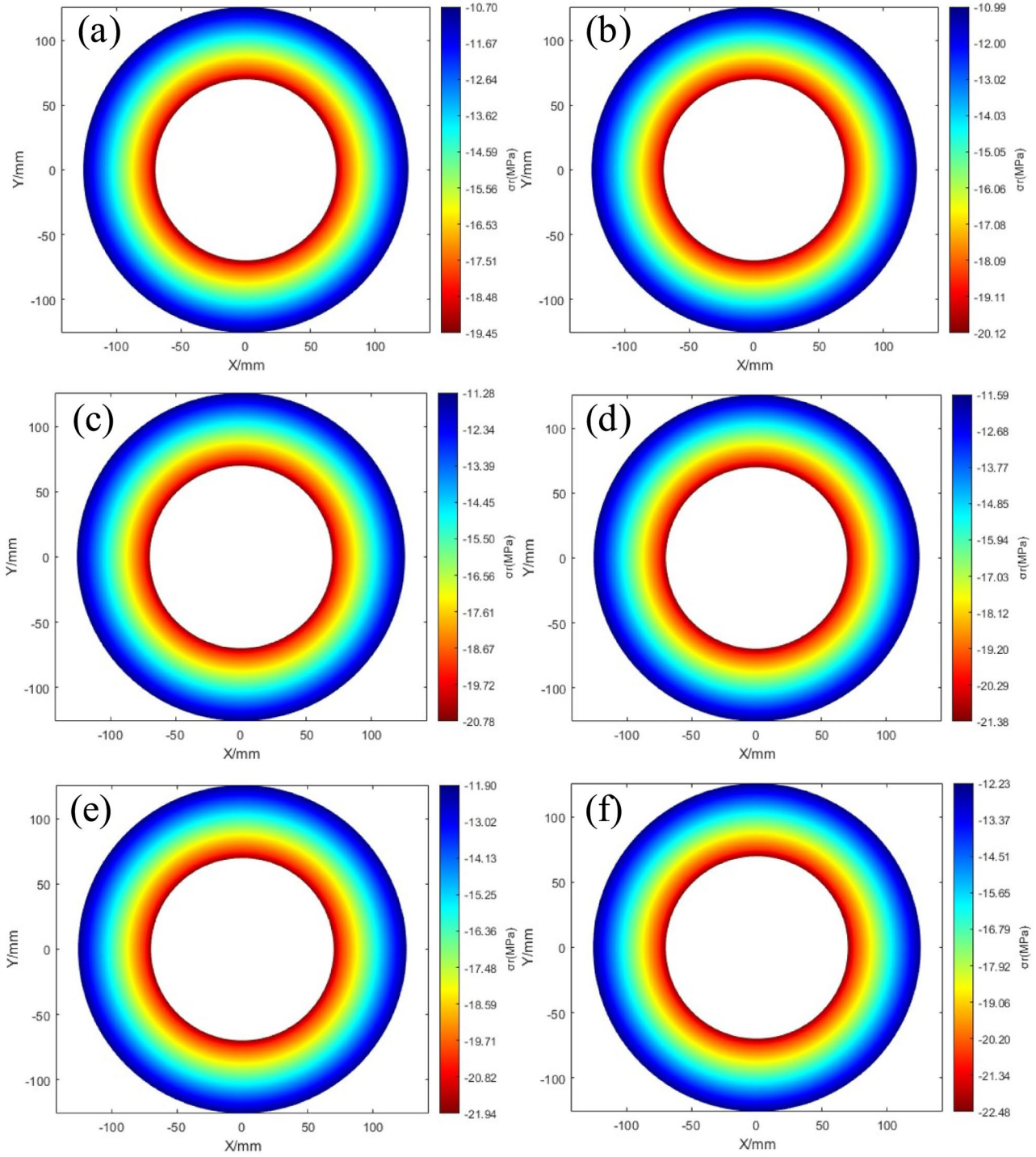

Fig. 9. (**a**) Radial stress nephogram of cement sheath with 5 mm CSCL thickness; (**b**) radial stress nephogram of cement sheath with 10 mm CSCL thickness; (**c**) radial stress nephogram of cement sheath with 15 mm CSCL thickness; (**d**) radial stress nephogram of cement sheath with 20 mm CSCL thickness; (**e**) radial stress nephogram of cement sheath with 25 mm CSCL thickness; (**f**) radial stress nephogram of cement sheath with 30 mm CSCL thickness.

Effect of casing wall thickness on corroded cement sheath

Different casing wall thicknesses were set to 5, 7.5, 10, 12.5, 15, and 17.5 mm, with an injection pressure of 60 MPa and a corrosion layer thickness of 5 mm. Other calculation parameters were configured according to the base case in Table 1. The radial stress of the cement sheath at the end of loading and the micro-annulus aperture after unloading under different casing wall thicknesses were calculated. Figure 12 shows the nephogram of radial stress in the cement sheath at the end of loading under different corrosion layer thicknesses, and the specific

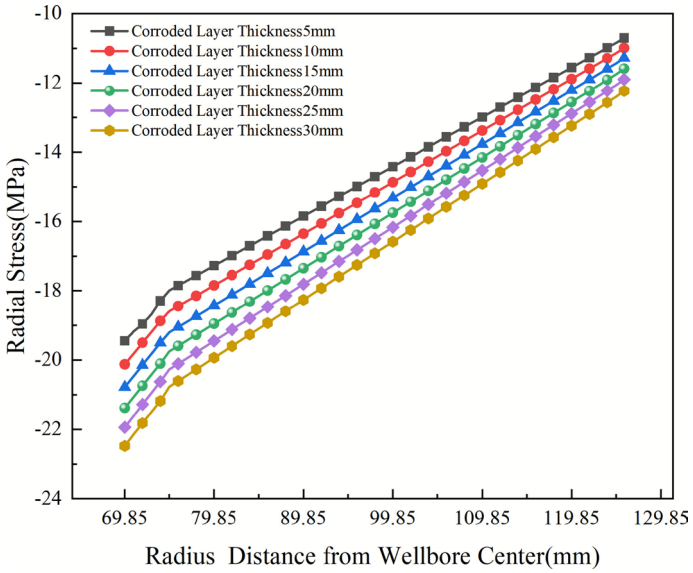

Fig. 10. Effects of differential CSCL thickness on cement sheath radial stress.

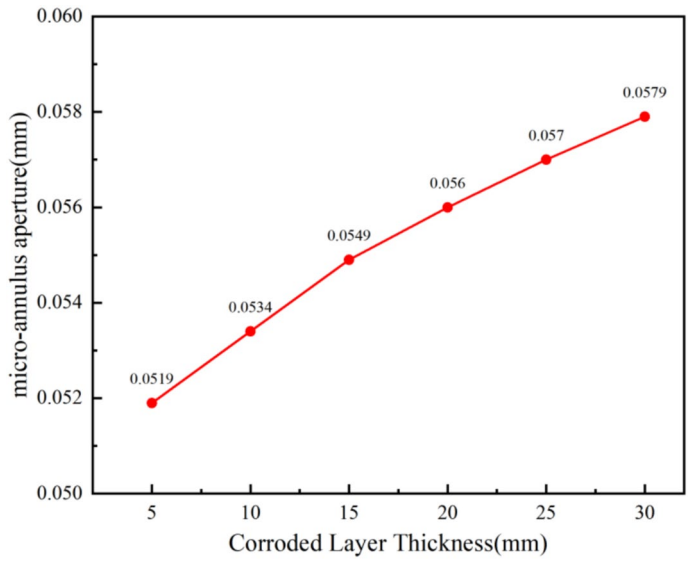

Fig. 11. Micro-annulus at primary cementing interface under differential CSCL thickness.

calculation results are presented in Figs. 13 and 14. As shown in Fig. 13, as the casing wall thickness increases, the radial stress in the cement sheath at the end of internal pressure loading decreases. When the casing wall thickness is 5 mm, the maximum radial stress in the cement sheath is -28.88 MPa. When the casing wall thickness increases to 17.5 mm, the maximum radial stress reduces to -18.68 MPa. Furthermore, as illustrated in Fig. 14, as the casing wall thickness increases from 7.5 mm to 17.5 mm, the micro-annulus aperture decreases, with the aperture at the primary cementing interface reducing from 0.1829 mm to 0.0413 mm. This indicates that increasing the casing wall thickness significantly reduces the maximum radial stress in the cement sheath and decreases the extent of plastic deformation. Under feasible CO_2 storage conditions, to minimize plastic deformation in the cement sheath, ensure its sealing integrity, and reduce the risk of CO_2 leakage through the cement sheath interface, it is advisable to select casings with larger wall thicknesses.

Discussion

This study established an analytical model based on elastoplastic mechanics to analyze the stress-displacement response and sealing integrity of cement sheaths containing a CO_2 corroded layer under injection-storage loading. The results indicate that CO_2 corrosion leads to significant degradation of the mechanical properties of the cement sheath, forming a weakened corroded layer. This corroded layer preferentially enters a plastic state under casing internal pressure loading, exhibiting significant differences in stress distribution and radial

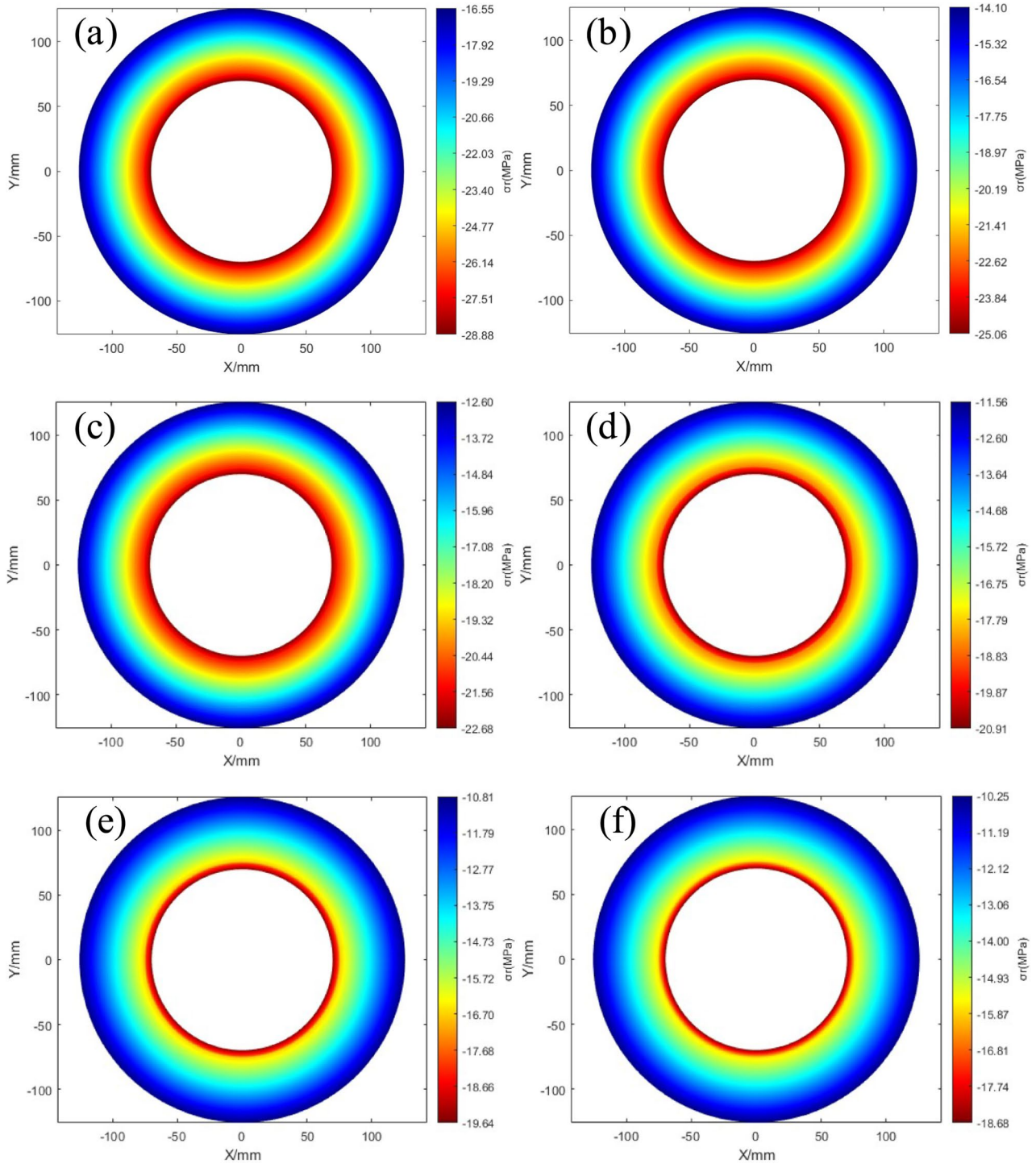

Fig. 12. (**a**) Radial stress nephogram of CCS with 5 mm casing wall thickness; (**b**) radial stress nephogram of CCS with 7.5 mm casing wall thickness; (**c**) radial stress nephogram of CCS with 10 mm casing wall thickness; (**d**) radial stress nephogram of CCS with 12.5 mm casing wall thickness; (**e**) radial stress nephogram of CCS with 15 mm casing wall thickness; (**f**) radial stress nephogram of CCS with 17.5 mm casing wall thickness.

displacement compared to an intact cement sheath. Through model solving, we quantified the influence of key operational parameters and material parameters on cement sheath integrity. The results show that as the corrosion layer thickness and the injection pressure difference increase, the risk of plastic yielding in the cement sheath increases significantly, making interfacial micro-annulus more likely to form, thereby exacerbating the risk of sealing failure.

Prior research has primarily focused on revealing the influence of CO_2 corrosion on the mechanical properties of cement stone itself, providing a critical foundation for determining the mechanical parameters of

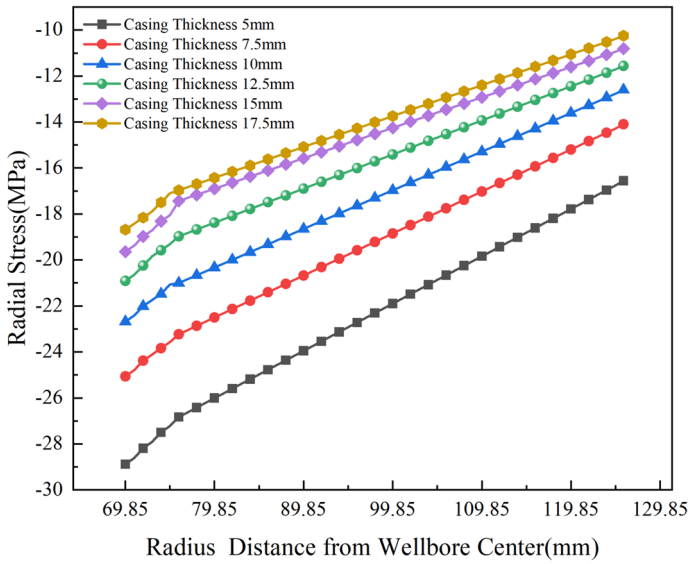

Fig. 13. Effects of differential casing wall thickness on cement sheath radial stress.

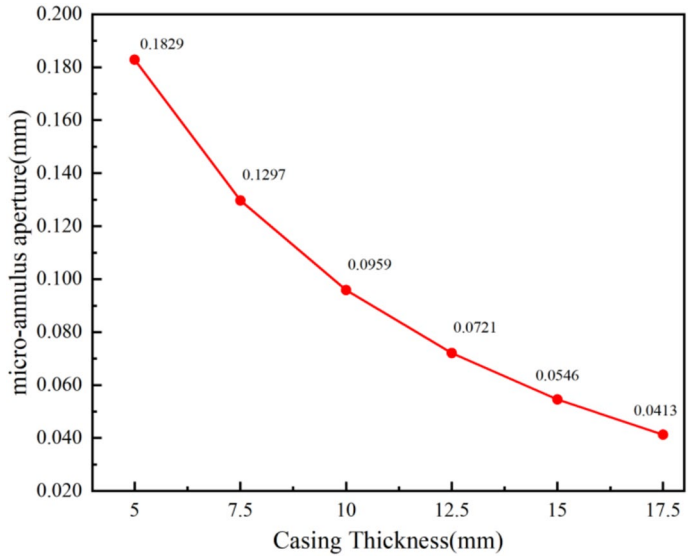

Fig. 14. Micro-annulus at primary cementing interface under differential casing wall thickness.

the CSCL this study. However, as noted in the introduction of this paper, most existing studies rely on numerical simulations to analyze the coupled effects of corrosion and mechanical loading, lacking a theoretical model capable of clearly elucidating the physical mechanisms underlying failure. In contrast to purely numerical simulations, the elastoplastic analytical model established in this study based on thick-walled cylinder theory and the Mohr–Coulomb criterion enables quantitative characterization of stress and displacement evolution in cement sheath during CO_2 storage processes. Utilizing this model, we can precisely identify the critical locations, where yielding first occurs within the cement sheath, thereby revealing the origins of sealing failure more profoundly, rather than merely presenting the final failure outcomes.

Although this study has made significant advancements in theoretical modeling, several limitations remain. The model treats the material as an ideal elastoplastic body and assumes the corrosion layer is uniform and continuous. It should be noted that the present model uses an ideal elastoplastic constitutive law based on the Mohr–Coulomb criterion, characterized by a small set of parameters for both intact and corroded cement. This choice enables closed-form analytical solutions, but it cannot fully describe the complex behavior of corroed cement during long-term service, such as stiffness degradation, damage evolution, microcrack propagation and residual strain accumulation under cyclic loading. In reality, CO_2 corrosion of cement often exhibits non-uniform characteristics, resulting in a porous, discontinuous gradient damage structure. Representing the CSCL as a homogeneous concentric ring smooths out these local heterogeneities and tends to underestimate stress and

strain concentrations near weak spots. As a consequence, the predicted radial tensile stress and micro-annulus aperture should be interpreted as spatially averaged values and may represent a lower bound compared with wells that exhibit strongly localized corrosion paths. Secondly, the model primarily focuses on the coupling between mechanical loading and changes in material properties after corrosion, without comprehensively accounting for thermal stresses during injection/storage or the dynamic evolution of material properties caused by ongoing CO_2 corrosion chemical reactions. Furthermore, while the study provides theoretical solutions and numerical case studies with parameters sourced from Reference 26, the model predictions still require validation through targeted full-scale physical experiments.

To overcome the aforementioned limitations, future research could consider the following solutions:

(1) The corrosion layer could be further discretized into multiple concentric rings with distinct mechanical parameters to simulate gradient variations in mechanical properties, thereby more accurately capturing non-uniform corrosion effects.
(2) A fluid–solid-thermal-chemical multi-field coupling model should be established to integrate multi-physics solutions for wellbores during long-term CO_2 storage. This would predict the time-dependent degradation of cement sheath performance and its impact on sealing integrity under prolonged service conditions.
(3) Full-scale CO_2 corrosion physical simulation experiments should be designed to measure the strain field and interfacial sealing pressure of cement sheaths with corrosion defects under cyclic internal pressure. Measured data should be compared with model predictions to calibrate and validate model accuracy.

The core future objective should be developing a life prediction methodology based on reliable models. By integrating corrosion kinetics models with this mechanical model and incorporating reliability engineering theory, it becomes possible to predict the reliability of the cement sheath's sealing function at various corrosion stages under specific schemes. This provides a direct scientific basis for risk management and maintenance decision-making in CCUS wells.

Conclusion

This research aims to analyze the sealing integrity of cement sheaths subjected to CO_2 corrosion under long-term conditions during CO_2 geological storage. The following conclusions are drawn:

(1) Based on the fundamental theory of elastoplastic mechanics, a mechanical model of the casing-CCS (corroded cement sheath)-formation assembly was established. This model integrates thick-walled cylinder theory and the Mohr–Coulomb criterion to quantitatively characterize the stress-displacement responses of the assembly under CO_2 injection and storage conditions.
(2) CO_2-induced corrosion causes significant degradation in the mechanical properties of the cement sheath, increasing its susceptibility to sealing integrity failure. Compared to an uncorroded cement sheath, a CCS with a 5 mm corroded layer subjected to 60 MPa injection pressure exhibits higher radial compressive stress and larger plastic deformation, and the micro-annulus aperture at the primary interface after unloading increases from 0.0238 mm to 0.0519 mm (an increase of 118%).
(3) Using the developed mechanical model, the effects of varying injection pressures, corrosion layer thicknesses, and casing wall thicknesses on cement sheath integrity were evaluated. As the injection pressure increases from 40 to 100 MPa, the micro-annulus aperture grows from 0.0211 mm to 0.1113 mm. In contrast, increasing the CSCL thickness from 5 to 30 mm only enlarges the aperture from 0.0519 mm to 0.0579 mm (11.5%), while increasing casing wall thickness from 7.5 mm to 17.5 mm reduces it from 0.1829 mm to 0.0413 mm. This highlights the importance of injection pressure management and the use of thicker casings for long-term integrity assurance.

These findings provide a theoretical foundation for optimizing wellbore design in CCUS (carbon capture, utilization and storage) projects, emphasizing operational controls (pressure management) and mechanical reinforcements (thicker casing) to ensure long-term sealing performance against CO_2-induced degradation.

Data availability

Data available on request from the corresponding author.

Received: 3 November 2025; Accepted: 29 January 2026
Published online: 13 February 2026

References

1. Dai, S., Liao, T. & Wu, Y. Progress of CO_2 geological storage research, policy development and suggestions in China. *Carbon Manag.* **16**, 14. https://doi.org/10.1080/17583004.2025.2485104 (2025).
2. Li, X. & Fang, Z. Status quo of connection technologies of CO2 geological storage in China. *Rock Soil Mech.* **28**, 2229 (2007).
3. Du, J., Zhou, A., Zhong, Y. & Shen, S. Molecular simulation on CO2 adsorption heterogeneity in montmorillonite nanopores with different surface charges in presence of water. *Chem. Eng. J.* **482**, 14. https://doi.org/10.1016/j.cej.2024.148958 (2024).
4. Leung, D., Caramanna, G. & Maroto-Valer, M. An overview of current status of carbon dioxide capture and storage technologies. *Renew. Sust. Energ. Rev.* **39**, 426–443. https://doi.org/10.1016/j.rser.2014.07.093 (2014).
5. Bachu, S. Sequestration of CO_2 in geological media: criteria and approach for site selection in response to climate change. *Energy Convers. Manage.* **41**, 953–970. https://doi.org/10.1016/s0196-8904(99)00149-1 (2000).
6. White, C., Strazisar, B., Granite, E., Hoffman, J. & Pennline, H. Separation and capture of CO_2 from large stationary sources and sequestration in geological formations -: Coalbeds and deep saline aquifers. *J. Air Waste Manage. Assoc.* **53**, 645–715. https://doi.org/10.1080/10473289.2003.10466206 (2003).

7. Hong, Z. et al. A quick method for appraising pore connectivity and ultimate imbibed porosity in shale reservoirs. *J. Marine Sci. Eng.* **13**, 174 (2025).
8. Meng, M. et al. Rock Fabric of Lacustrine Shale and Its Influence on Residual Oil Distribution in the Upper Cretaceous Qingshankou Formation Songliao Basin. *Energy Fuels* **37**, 7151–7160. https://doi.org/10.1021/acs.energyfuels.3c00527 (2023).
9. Loizzo, M. *et al.* in *10th International Conference on Greenhouse Gas Control Technologies.* 5203–5210 (Elsevier Science Bv, 2011).
10. Wang, D. et al. CO2 sequestration wells sealing evaluation model: Jimusar depression, China as an example. *Geoenergy Sci. Eng* https://doi.org/10.1016/j.geoen.2024.213439 (2025).
11. Bai, M., Sun, J., Song, K., Reinicke, K. & Teodoriu, C. Evaluation of mechanical well integrity during CO_2 underground storage. *Environ. Earth Sci.* **73**, 6815–6825. https://doi.org/10.1007/s12665-015-4157-5 (2015).
12. Li, C. et al. A new method to protect the cementing sealing integrity of carbon dioxide geological storage well: An experiment and mechanism study. *Eng. Fracture Mech.* https://doi.org/10.1016/j.engfracmech.2020.107213 (2020).
13. Li, J., Chen, Y., Liang, W., Zhang, S. & Qiu, Y. Experimental investigation on permeability and mechanical properties of cement-salt rock interface subjected to cyclic loading. *Rock Mech. Rock Eng.* **56**, 7281–7299. https://doi.org/10.1007/s00603-023-03434-9 (2023).
14. Zhou, S. et al. Mechanical characteristics of well cement under cyclic loading and its influence on the integrity of shale gas wellbores. *Fuel* **250**, 132–143. https://doi.org/10.1016/j.fuel.2019.03.131 (2019).
15. Udebhulu, O., Aladeitan, Y., Azevedo, R. & De Tomi, G. A review of cement sheath integrity evaluation techniques for carbon dioxide storage. *J. Petroleum Explor. Product. Technol.* **14**, 1–23. https://doi.org/10.1007/s13202-023-01697-0 (2024).
16. Deng, K. et al. Failure mechanism and influencing factors of cement sheath integrity under alternating pressure. *Pet. Sci.* **20**, 2413–2427. https://doi.org/10.1016/j.petsci.2023.03.004 (2023).
17. Chu, W., Shen, J., Yang, Y., Li, Y. & Gao, D. Calculation of micro-annulus size in casing-cement sheath-formation system under continuous internal casing pressure change. *Pet. Explor. Dev.* **42**, 414–421. https://doi.org/10.1016/s1876-3804(15)30033-1 (2015).
18. Zhang, X. et al. Study on the sealing integrity of cement sheath under cyclic internal pressure considering temperature effects. *Geoenergy Sci. Eng.* https://doi.org/10.1016/j.geoen.2025.213761 (2025).
19. Zhang, H., Shen, R., Yuan, G., Ba, Z. & Hu, Y. Cement sheath integrity analysis of underground gas storage well based on elastoplastic theory. *J. Petrol. Sci. Eng.* **159**, 818–829. https://doi.org/10.1016/j.petrol.2017.10.012 (2017).
20. Xi, Y., Lian, W., Fan, L., Tao, Q. & Guo, X. Research and engineering application of pre-stressed cementing technology for preventing micro-annulus caused by cyclic loading-unloading in deep shale gas horizontal wells. *J. Petroleum Sci. Eng.* https://doi.org/10.1016/j.petrol.2021.108359 (2021).
21. Zhou, S. et al. Study on the mechanism and controlling method for annulus pressure buildup problems in shale gas wells. *Geoenergy Sci. Eng.* https://doi.org/10.1016/j.geoen.2023.212065 (2023).
22. Su, D. et al. Mechanical property design method of cement sheath in a horizontal shale oil well under fracturing conditions. *Pet. Explor. Dev.* **49**, 919–928. https://doi.org/10.1016/s1876-3804(22)60321-5 (2022).
23. Su, D. et al. Sealing integrity evaluation and optimization of cement sheath-formation interface under different formation conditions during fracturing. *J. Earth Sci.* **36**, 223–232. https://doi.org/10.1007/s12583-023-1837-z (2025).
24. Zhou, N. et al. Damage behavior and constitutive model of cement sheath under alternating temperature. *Geoenergy Sci. Eng.* https://doi.org/10.1016/j.geoen.2025.213945 (2025).
25. Yuan, B., Luo, W., Xu, B. & Fan, H. A prediction model for carbonation depth of cement sheath of carbon capture utilization and storage (CCUS) wells. *J. Nat. Gas Sci. Eng.* https://doi.org/10.1016/j.jngse.2022.104842 (2022).
26. Kutchko, B., Strazisar, B., Lowry, G., Dzombak, D. & Thaulow, N. Rate of CO_2 attack on hydrated Class H well cement under geologic sequestration conditions. *Environ. Sci. Technol.* **42**, 6237–6242. https://doi.org/10.1021/es800049r (2008).
27. Wu, Z., Wu, G. & Xing, X. Sealing integrity of cement sheath under the condition of CO_2 corrosion-stress coupling. *Drilling Fluid Completion Fluid.* **41**, 220–230 (2024).
28. Gu, T. et al. Coupled effect of CO_2 attack and tensile stress on well cement under CO_2 storage conditions. *Constr. Build. Mater.* **130**, 92–102. https://doi.org/10.1016/j.conbuildmat.2016.10.117 (2017).
29. Mei, K. et al. Effectiveness and microstructure change of alkali-activated materials during accelerated carbonation curing. *Constr. Build. Mater.* https://doi.org/10.1016/j.conbuildmat.2020.122063 (2021).
30. Li, Y., Tang, H., Wu, P. & Song, Y. Micro mechanical behavior and strain localization of oil well cement corroded by CO2. *Constr. Build. Mater.* https://doi.org/10.1016/j.conbuildmat.2024.138371 (2024).
31. Zhang, H. et al. Application of ABAQUS Flow-Solid coupling model to evaluate sealing capability of sandstone formation interface based on the cracking behavior of cohesive force units. *Constr. Build. Mater.* **409**, 19. https://doi.org/10.1016/j.conbuildmat.2023.133863 (2023).
32. Bu, Y. et al. Stress concentration of perforated cement sheath and the effect of cement sheath elastic parameters on its integrity failure during shale gas fracturing. *Front. Mater.* **9**, 14. https://doi.org/10.3389/fmats.2022.980920 (2022).
33. He, Y., Song, Y., Hu, S., Liu, H. & Ge, X. Mechanical evaluation of casing in multiple thermal recovery cycles for offshore heavy oil wells. *J. Marine Sci. Eng.* https://doi.org/10.3390/jmse13030597 (2025).

Author contributions

K.Z. and H.M analyzed most of the data and wrote the main manuscript text. S.Z. contributed the central idea, revised the first draft, and provided financial support. Z.R. and Y.Z assisted with the analysis of the model and results. D.F. prepared all figures. All authors reviewed the manuscript.

Funding

This work is supported by National Natural Science Foundation of China (Grant No. 52404002), Open Fund of Hubei Key Laboratory of Oil and Gas Drilling and Production Engineering (Yangtze University) (Grant No. YQZC202411).

Declarations

Competing interests

The authors declare no competing interests.

Additional information

Correspondence and requests for materials should be addressed to S.Z.

Reprints and permissions information is available at www.nature.com/reprints.